Journal of Catalysis 324 (2015) 69–78

Contents lists available at ScienceDirect

Journal of Catalysis

journal homepage: www.elsevier.com/locate/jcat

Promoted ceria catalysts for alkyne semi-hydrogenation

Gianvito Vilé [a], Patrick Dähler [a], Julia Vecchietti [b], Miguel Baltanás [b], Sebastián Collins [b], Mónica Calatayud [c,d,e], Adrian Bonivardi [b,*], Javier Pérez-Ramírez [a,*]

[a] Institute for Chemical and Bioengineering, Department of Chemistry and Applied Biosciences, ETH Zurich, Vladimir-Prelog-Weg 1, 8093 Zurich, Switzerland
[b] Institute for the Technological Development of the Chemical Industry, Universidad Nacional del Litoral and CONICET, Güemes 3450, 3000 Santa Fe, Argentina
[c] Sorbonne Universites, UPMC Univ Paris 06, UMR 7616, Laboratoire de Chimie Théorique, 75005 Paris, France
[d] CNRS, UMR 7616, Laboratoire de Chimie Théorique, 75005 Paris, France
[e] Institut Universitaire de France, France

ARTICLE INFO

Article history:
Received 11 October 2014
Revised 21 January 2015
Accepted 22 January 2015

Keywords:
Alkyne hydrogenation
Olefin production
Promoted ceria
Gallium
Indium
H_2 activation

ABSTRACT

CeO_2 is a highly selective catalyst for the partial hydrogenation of alkynes. However, due to its limited H_2 splitting ability, a high operating temperature is required for the reaction, hampering the practical exploitation of this abundant oxide. In this work, we demonstrate that gallium promotes the activity of CeO_2 for the semi-hydrogenation of acetylene and methylacetylene, enabling a reduction of the operating temperature to 373 K, while maintaining an outstanding ethylene and propylene selectivity (80–97%), even in the presence of excess alkene in the feed. Oligomers comprised the main secondary product, while the selectivity to the corresponding alkane did not exceed 2%. The characterization of mixed Ce-Ga oxides reveals that the progressive incorporation of gallium into the ceria structure, forming a solid solution, boosts the oxygen storage capacity and the reducibility of the material. This is ascribed to the facilitated H_2 activation on the Ga-promoted samples, as confirmed by *in situ* infrared spectroscopy and density functional theory simulations. The interplay between the advantage brought by the decreased barrier for H_2 cleavage and the disadvantage due to the increased number of oxygen vacancies governs the reactivity of the $CeGaO_x$ catalysts in alkyne hydrogenation. The composition in the optimal catalyst, containing a molar Ce:Ga ratio of 95:5, was extrapolated to other trivalent cations. Indium incorporated in the ceria lattice favored the low-temperature H_2 activation and led to an activity enhancement that surpassed that of gallium. However, aluminum did not form a solid solution with ceria and caused no effect. This work comprises the first application of promoted cerias in hydrogenation catalysis and may prompt further developments in olefin purification.

1. Introduction

As the most abundant rare earth oxide, cerium (IV) oxide (ceria, CeO_2) has attracted significant interest over the past decades. Undoubtedly, major applications are found in oxidation catalysis, where CeO_2 is used as a promoter or main active phase in the automotive gas emissions conversion, abatement of volatile organic compounds, soot oxidation, and chlorine recovery [1–4]. Recently, the benefits of ceria in methanol synthesis and water–gas shift catalysts have been reported [5,6]. The impact of ceria in these transformations originates from its high oxygen storage capacity (OSC) and the ability to switch between the Ce^{4+} and Ce^{3+} valence states, storing and releasing oxygen ions [7]. As demonstrated in pioneering works by Nowick et al. in the late 1970s [8], the introduction of a metal into the ceria lattice is an efficient and versatile way of further enhancing these unique properties. The guest metal (often referred to as promoter or dopant) disturbs the fluorite structure of CeO_2 and alters the local defect configuration, affecting the ionic conductivity of the material [9,10]. At high temperature, this increases the mobility of the oxygen species. It has been shown that ceria catalysts modified with minute amount of lanthanum, zirconium, or hafnium exhibit a lower energy for the creation of oxygen vacancies, which boosts the redox behavior and thus the oxidation activity [11,12]. The charge of the promoter, however, has a marked influence on the properties of ceria. It is known that tetravalent cations mainly affect the relaxation energy of the oxide, whereas trivalent cations may induce electronic changes together with structural relaxation effects [9].

The recent discovery of CeO_2 as a highly selective catalyst for the gas and liquid-phase hydrogenation of acetylenic compounds

* Corresponding authors.
E-mail addresses: abonivar@santafe-conicet.gov.ar (A. Bonivardi), jpr@chem.ethz.ch (J. Pérez-Ramírez).

http://dx.doi.org/10.1016/j.jcat.2015.01.020
0021-9517/

has opened new perspectives in catalysis beyond oxidation [13,14]. The hydrogenation of alkynes is an important step for the industrial synthesis of polymer-grade olefins and pharmaceutical intermediates, and is generally performed over modified palladium catalysts [15,16]. The practical relevance of this reaction has led to intense efforts to design novel catalytic systems with the purpose of maximizing the alkene selectivity [17–19]. Density functional theory (DFT) calculations have ascribed the high olefin selectivity of CeO_2 to the role of the oxygen species (active sites) in stabilizing reactive intermediates, their isolation, largely suppressing oligomerization pathways, and the high energy barrier for the over-hydrogenation step [20]. However, similar to other catalytic systems [19], the reaction requires a 200 K higher operating temperature than the state-of-the-art palladium, owing to the limited ability of ceria to activate H_2 [20,21]. This curbs the practical exploitation of the much cheaper oxide since the material cannot retrofit existing plants for olefin purification. Besides, at high temperature (>550 K) under H_2 flow, the activity of ceria drops dramatically due to the formation of oxygen vacancies on the surface. In contrast to oxidation catalysis, these are detrimental in hydrogenation, as they reduce the amount of active sites [22].

The use of promoters to boost the activity of ceria in hydrogenation catalysis has not been demonstrated to date. Gallium is an excellent candidate to tackle this problem, due to its reported ability to increase the reducibility of ceria and to facilitate the H-H bond cleavage [23–25]. Herein, we demonstrate that the presence of gallium boosts the activity of ceria for the semi-hydrogenation of acetylene and methylacetylene. The role of gallium is rationalized through the combination of catalytic testing, characterization by *in situ* infrared spectroscopy, and mechanistic studies using density functional theory simulations. A fine balance between the facilitated H_2 activation and the creation of vacancies, attained by content of Ga in the mixed cerium-gallium oxide, leads to an optimal catalytic performance. Following this principle, indium was also identified as a highly effective promoter.

2. Experimental

2.1. Catalyst preparation

Cerium oxide (CeO_2), gallium oxide (Ga_2O_3), and gallium-containing ceria catalysts with a nominal atomic Ce:Ga ratio of 99:1, 98:2, 95:5, 90:10, and 80:20 (coded $Ce_{99}Ga_1O_x$, $Ce_{98}Ga_2O_x$, $Ce_{95}Ga_5O_x$, $Ce_{90}Ga_{10}O_x$, and $Ce_{80}Ga_{20}O_x$, respectively) were prepared by co-precipitation of aqueous solutions of $Ce(NO_3)_3{\cdot}6H_2O$ (99.99%, Sigma–Aldrich) and $Ga(NO_3)_3{\cdot}9H_2O$ (99.999%, Sigma–Aldrich) with NH_4OH [23]. Briefly, the mixture of the nitrate solutions was slowly added to the ammonium hydroxide solution under vigorous stirring, keeping the pH at 8.5. The precipitates were filtered, washed with water, dried in air at 393 K for 8 h, and calcined at 723 K for 5 h (heating rate = 5 K min^{-1}). The same co-precipitation procedure was applied to prepare $Ce_{95}Al_5O_x$ and $Ce_{95}In_5O_x$, using $Al(NO_3)_3{\cdot}9H_2O$ (99%, Acros-Organics) and $In(NO_3)_3$ (99.999%, Strem Chemicals) as the metal precursors. The $Ce_{95}Ga_5O_x$ catalyst was also prepared by solid-state synthesis. Appropriate amounts of CeO_2 (Sigma–Aldrich, ref: 1001772767) and Ga_2O_3 (Strem Chemicals, ref: 23875600) were ball-milled at 500 rpm for 5 h (Retsch Planetary PM200), and the resulting powder was calcined at 823 K for 4 h using 5 K min^{-1}.

2.2. Catalyst characterization

The chemical composition of the samples was determined by X-ray fluorescence spectrometry (XRF), using an Orbis Micro-EDXRF analyzer equipped with a 35 kV Rh anode and a silicon drift detector. X-ray photoelectron spectroscopy (XPS) was performed on a hemispherical PHOIBOS 150 spectrometer, using monochromatic Al Kα radiation (200 W, 12 kV) and operating in the fixed analyzer transmission (FAT) mode (pass energy = 30 eV). A flood gun FG 15/40 was employed to compensate surface charging effects. Prior to the analysis, the sample was pretreated under Ar flow at 473 K for 15 min. X-ray diffraction (XRD) was measured in a Shimadzu XD-D1 diffractometer equipped with a Cu Kα (λ = 0.1541 nm) source. Data were recorded in the 2θ range of 20–100°, with an angular step size of 0.1° and a counting time of 50 s per step. Nitrogen sorption at 77 K was performed using a Micromeritics ASAP 2020 instrument after sample evacuation at 473 K for 2 h. High-resolution transmission electron microscopy (HRTEM) was undertaken in a FEI Tecnai F30 microscope operated at 300 kV. Energy-dispersive X-ray spectrometry (EDS) mapping was conducted in a Hitachi HD-2700 microscope operated at 200 kV. The materials were dispersed in ethanol in an ultrasonic bath; a few droplets of the suspension were poured onto a holey carbon-coated copper grid and completely dried prior to microscopic analyses. Temperature-programmed reduction in hydrogen (H_2-TPR) was conducted in a Micromeritics Autochem 2920 unit connected to a Pfeiffer Thermostar quadrupole mass spectrometer. The catalyst (*ca.* 0.2 g) was loaded into a U-shaped quartz microreactor, pre-treated under flowing 5 vol.% O_2/He (50 cm^3 min^{-1}) at 773 K for 1 h, and cooled to 473 K in He (20 cm^3 min^{-1}). The analysis was performed under flowing 5 vol.% H_2/Ar (50 cm^3 min^{-1}), ramping the temperature from 473 to 1023 K at 10 K min^{-1}. The oxygen storage capacity (OSC) was determined using a TA Q-600 thermobalance. The sample (*ca.* 0.1 g) was reduced in 5 vol.% H_2/Ar, ramping the temperature from 298 to 773 K at 10 K min^{-1}, purged in He at 773 K for 15 min, and oxidized in O_2 at 473 K for 15 min. Afterward, the catalyst was further reduced in 5 vol.% H_2/Ar, ramping the temperature from 473 to 773 K at 10 K min^{-1}. All flow rates were set at 60 cm^3 min^{-1}. Diffuse reflectance infrared Fourier transform (DRIFT) spectroscopy was carried out in a Nicolet 8700 spectrometer equipped with an Hg–Cd–Te detector, a Harrick high-temperature cell, and KBr windows. The sample was pre-reduced in H_2 flow, ramping the temperature from 298 to 623 K at 15 K min^{-1}, followed by sequential treatments in H_2, He, O_2, and He at 623 K for 10 min. The isothermal reduction experiment was conducted at 523–623 K in 30 cm^3 min^{-1} of pure H_2.

2.3. Catalytic tests

The gas-phase hydrogenation of acetylene and methylacetylene was studied in a continuous-flow fixed-bed micro-reactor (12 mm i.d.) using the following conditions: catalyst mass W_{cat} = 0.4 g (particle size = 0.2–0.4 mm), temperature T = 323–523 K, molar H_2:alkyne = 10–30 (alkyne concentration = 2.5 vol.%, He as balance gas), contact time τ = 0.3 s, and total pressure P = 1 bar. The hydrogenation of acetylene was also studied by co-feeding 10 vol.% ethylene. The activity of selected catalysts for ethylene or propylene hydrogenation was assessed using 2.5 vol.% alkene and a molar H_2:alkene ratio of 30. The reactor effluent was analyzed by an online gas chromatograph (Agilent GC7890A). The conversion of alkyne and the selectivity to alkene and alkane were calculated according to Eqs. (1)–(3):

$$X(\text{alkyne}) = (c_{in}(\text{alkyne}) - c_{out}(\text{alkyne}))/(c_{in}(\text{alkyne})) \quad (1)$$

$$S(\text{alkene}) = (c_{out}(\text{alkene}) - c_{in}(\text{alkene}))/(c_{in}(\text{alkyne}) - c_{out}(\text{alkyne})) \quad (2)$$

$$S(\text{alkane}) = (c_{out}(\text{alkane}))/(c_{in}(\text{alkyne}) - c_{out}(\text{alkyne})) \quad (3)$$

Table 1
Characterization data of the samples.

Sample	Ga:(Ce + Ga)[a] (–)	Ga content[b] (wt.%)	S_{BET}[c] ($m^2\ g^{-1}$)	a_{cell}[d] (nm)	$d_{Scherrer}$[e] (nm)	T_{sr}[f] (K)	OSC[g] (μmol O g^{-1})
CeO_2	0 (0)	0	62	0.5416	10	710	50
$Ce_{99}Ga_1O_x$	0.01 (0.01)	0.41	76	–	–	–	–
$Ce_{98}Ga_2O_x$	0.02 (0.02)	0.86	91	–	–	–	–
$Ce_{95}Ga_5O_x$	0.05 (0.05)	2.12	106	0.5397	6	700	175
$Ce_{90}Ga_{10}O_x$	0.10 (0.10)	4.26	108	–	–	–	–
$Ce_{80}Ga_{20}O_x$	0.20 (0.25)	8.85	100	0.5378	4	675	475
$Ce_{95}Al_5O_x$	0.05 (0.01)[h]	1.50[h]	87	0.5407	7	800	–
$Ce_{95}In_5O_x$	0.05 (0.05)[h]	3.59[h]	34	0.5385	12	600	–

[a] Bulk ratio by XRF and, in brackets, surface ratio by XPS.
[b] XRF.
[c] Total surface area, BET method.
[d] Cell parameter, XRD.
[e] Average crystallite size, XRD.
[f] Temperature of surface reduction, H_2-TPR.
[g] Oxygen storage capacity, TGA in H_2 flow at 473 K.
[h] Values referred to aluminum or indium.

where $c_{in}(i)$ and $c_{out}(i)$ are, respectively, the inlet and outlet concentration of i, and in particular, in the absence of alkene in the feed mixture, c_{in}(alkene) equals to zero. The selectivity to oligomers was obtained through the carbon balance, considering that S(oligomers) = 100 − S(alkane) − S(alkene). This assumption is acceptable, taking into account the low tendency of the catalyst to coking (weight losses <3 wt.% were determined in the used catalysts by thermogravimetric analysis in air). The turnover frequency in alkyne semi-hydrogenation was expressed as mole of alkene per unit of time, n_{out}(alkene), and mole of active sites (that is, surface oxygens on the ceria phase) [20], taking into account the mass of the catalyst, m_{cat}, the surface area, S_{BET}, the catalyst surface density determined from XRD, ρ_{surf}, the surface Ce:(Ce + Ga) ratio, $r_{Ce,surf}$, the stoichiometry of the single oxides, and the Avogadro number, N_{Av}:

$$TOF = (n_{out}(\text{alkene}) \times N_{Av})/(m_{cat} \times S_{BET} \times \rho_{surf} \times r_{Ce,surf} \times 2) \quad (4)$$

This was regarded as the most suitable way of expressing the activity, considering that the catalysts have different surface areas and guest metal contents (Table 1).

3. Computational details

DFT + U calculations on H_2 activation were performed with the Vienna Ab initio Simulation Package code (v5.2.11) [26–28], using the Perdew–Burke–Ernzerhof functional [29]. Projector-augmented wave pseudo-potentials represented the core electrons (H, C(s), O(s), Ga(d), and Ce) [30,31], whereas a plane wave basis set with a kinetic cutoff energy of 300 eV described the valence electrons (H: $1s^1$, C: $2s^2\ 2p^2$, O: $2s^2\ 2p^4$, Ga: $4s^2\ 4p^1\ 3d^{10}$, and Ce: $6s^2\ 5d^1\ 4f^1$). This setting has been tested for determining the bulk lattice parameters (Fig. S1). All calculations were spin-polarized; particularly, the Hubbard U-like term describing the on-site Coulomb interactions was included in order to describe the Ce 4f states ($U - J$ = 5 eV) [32]. The electronic relaxation was converged until the energy differences were below 0.1 meV. The conjugate-gradient algorithm was used for geometry optimization, with a threshold for the ionic relaxation of 1 meV. The adsorbates together with the two uppermost slab CeO_2 layers were allowed to relax, while the two bottom CeO_2 slab layers were kept fixed to bulk positions. The k-point mesh used was 0.05 $Å^{-1}$ in the reciprocal space (Monkhorst–Pack 2 × 2 × 1). Transition states were located through the climbing-image version of the nudged elastic band algorithm [33], and a vibrational analysis of the potential transition state structure was performed to fully characterize the saddle points. For these calculations, only selected atoms were allowed to relax (H_2 molecule and neighboring atoms). The 3 × 3 (1 1 1) termination of the fluorite CeO_2 structure was chosen to model the slab. The gallium-containing slab was modeled by replacing one surface cerium by a gallium site; one hydrogen atom was included to keep formal charges as Ce^{4+}, Ga^{3+}, O^{2-}, and H^+. The compositions of the slabs were $Ce_{36}O_{72}$ for pure ceria and $Ce_{35}GaO_{72}H$ for gallium-promoted ceria, corresponding to Ce:Ga = 97:3.

4. Results and discussion

4.1. Catalyst characterization

There is an extensive literature on synthetic methods that can be applied for preparing promoted ceria catalysts. The most employed techniques are solid-state synthesis, flame combustion, co-precipitation, sol–gel synthesis, ultrasonic spray pyrolysis, and electrochemical deposition [10]. In all cases, the control of the preparation method can guarantee to produce a truly homogeneous incorporation of the promoter into the ceria phase, avoiding the deposition of small clusters of the guest metal on the surface [34]. In this work, the promoted CeO_2 catalysts were primarily synthesized by co-precipitation. This method has been successfully applied for preparing Zr, Ta, and Nb-containing CeO_2 [35,36]. The chemical composition and textural properties of the mixed Ce-Ga solid oxides are summarized in Table 1, and compared with those of pure CeO_2. The total concentration of Ga in the catalysts, determined by XRF, ranges between 0.4 and 8.8 wt.%, and no considerable difference between the bulk and the surface Ga:(Ce + Ga) ratio is noticed. XRF also confirmed the high purity of the materials, which contain no traces of other metals. The XRD patterns (Fig. 1a) exhibit relatively broad reflections that can be indexed to the fluorite structure of ceria; no phase separation is detected, even at the highest concentration of gallium in the samples. The average crystallite size of pure CeO_2, calculated by the Scherrer equation, is *ca.* 10 nm. Smaller crystallites are obtained in the gallium-containing samples (*ca.* 6 nm for $Ce_{95}Ga_5O_x$ and 4 nm for $Ce_{80}Ga_{20}O_x$), in line with the increased total surface area of the promoted oxides, which reaches values around 100 $m^2\ g^{-1}$ (Table 1). A shift to higher angles of the characteristic ceria reflections is noticed over the Ga-containing materials, pointing to the formation of the corresponding solid solutions. The lattice parameters of $Ce_{95}Ga_5O_x$ (a_{cell} = 0.5397 nm) and $Ce_{80}Ga_{20}O_x$ (a_{cell} = 0.5378 nm) are smaller than that of CeO_2 (a_{cell} = 0.5463 nm); the shrinkage of the lattice further confirms the substitution of Ce^{4+} with Ga^{3+} in the fluorite lattice. The catalysts were also characterized by

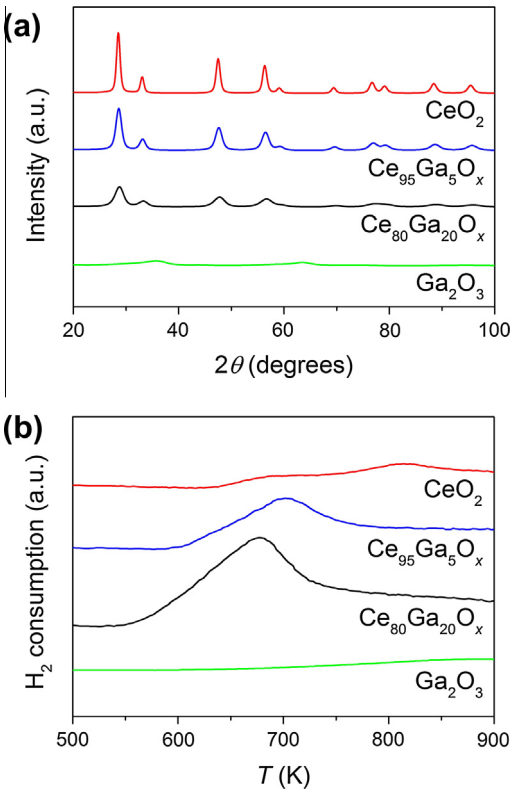

Fig. 1. X-ray diffraction patterns (a) and H_2-TPR profiles (b) of the Ga-promoted ceria catalysts and the pure oxides.

transmission electron microscopy (Fig. 2). The crystals exhibit a truncated octahedron-like morphology and form small agglomerates. The micrographs further confirm the decreased particle size in the gallium-containing samples. The selected-area diffraction patterns in the insets reveal that the Ga-promoted catalysts have the fluorite structure of ceria. The elemental maps in Fig. 3 show the uniform distribution of Ce and Ga within the particles, further supporting the presence of $CeGaO_x$ solid solutions, even at the highest gallium content, as well as the absence of small CeO_2 or Ga_2O_3 clusters on the surface of the catalyst. The H_2-TPR profiles in Fig. 1b show a characteristic peak at around 600–800 K, assigned to the reduction of surface oxygen species [4]. This peak shifts to lower temperatures when the concentration of gallium is increased, as also indicated by the temperature of surface reduction in Table 1, suggesting that gallium enhances the reducibility of ceria. Determination of the oxygen storage capacity, OSC, by thermogravimetric analysis supports these results, revealing that the mixed $CeGaO_x$ oxides can store up to ten times more oxygen than pure CeO_2 (Table 1). This result indicates the much greater reducibility of Ce^{4+} in the gallium-promoted cerias [23,25].

4.2. Activation of H_2

In an attempt to understand the improved reducibility of $CeGaO_x$, periodic density functional theory calculations were performed. Different reaction pathways for the dissociation of molecular H_2 were analyzed. The possible species are detailed in Fig. S1 and, for the sake of clarity, only the most favorable configuration is described in the manuscript. The energy profile on pure and Ga-containing ceria is displayed Fig. 4a. The reaction starts with the adsorption of molecular hydrogen. This step is exothermic and

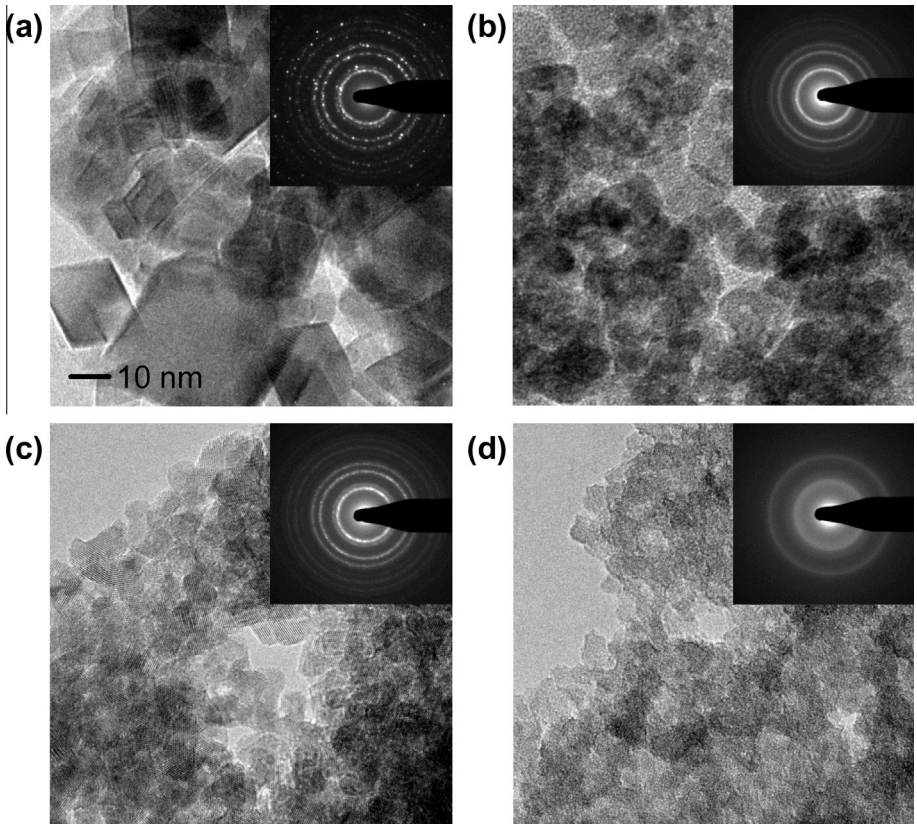

Fig. 2. High-resolution transmission electron microscopy of CeO_2 (a), $Ce_{95}Ga_5O_x$ (b), $Ce_{80}Ga_{20}O_x$ (c), and Ga_2O_3 (d). The electron diffraction patterns in the insets evidence that the promoted ceria catalysts have the fluorite structure. The scale bar applies to all micrographs.

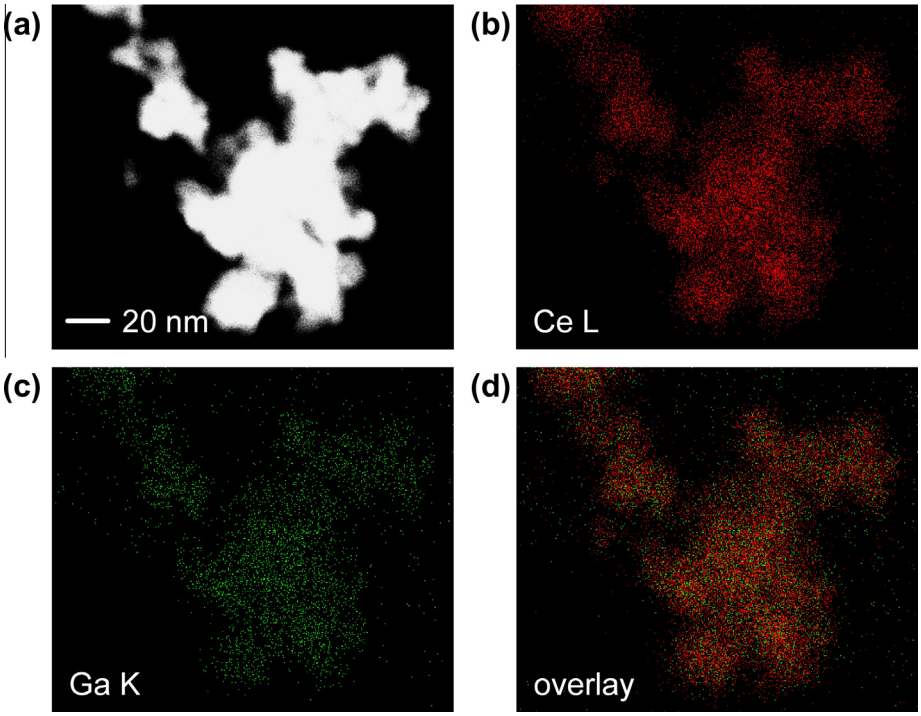

Fig. 3. *Z*-contrast transmission electron micrograph of $Ce_{80}Ga_{20}O_x$ (a) and respective energy-dispersive X-ray spectroscopy elemental mapping of Ce (b) and Ga (c), and the Ce and Ga overlay map (d).

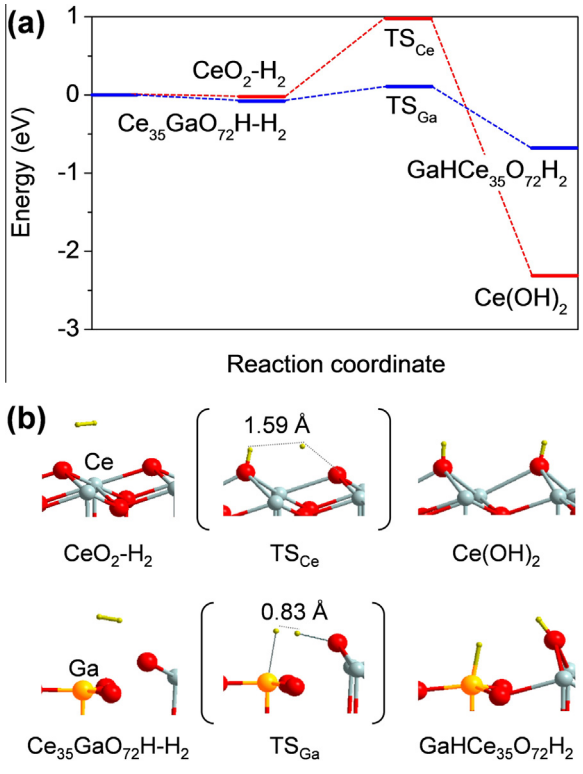

Fig. 4. Energy profile of the activation of hydrogen on CeO_2(1 1 1) and $Ce_{35}GaO_{72}H$ (a) and the corresponding most stable structures for the initial, transition, and final states of the reaction (b).

releases 0.02 eV (2 kJ mol^{-1}) over CeO_2 and 0.08 eV (8 kJ mol^{-1}) over $CeGaO_x$. The transition structures involve the stretching and splitting of the H-H bond; the corresponding activation energies are 1.00 eV (96 kJ mol^{-1}) over CeO_2 and only 0.19 eV (18 kJ mol^{-1}) over Ga-containing CeO_2; the former value, in particular, is in agreement with the literature [21,37]. The much lower activation energy over $CeGaO_x$ can be correlated with the distance of the H-H bond in the transition state configuration (Fig. 4b): this distance is 0.83 Å over the Ce-Ga solid solution, which represents only a small elongation with respect to the gas-phase H-H bond (0.74 Å). This value is considerably smaller than that found over pure ceria (1.59 Å). It should be stressed that, in the case of ceria, we have modeled the homolytic dissociation of H_2 on two oxygen species. Recently, an alternative mechanism involving the heterolytic splitting of H_2, favored by the surface electrostatic field between the Ce and O centers, and forming CeH hydride and OH intermediates, has been reported. According to García-Melchor and López [21], the CeH/OH pair is 0.75 eV higher in energy than the reference (0.55 eV in our model) and leads to a transition state with the H-H distance of 1.29 Å. The transition state energy leading to the final hydroxyl groups (OH/OH pairs) is 1.08 eV, whereas that of the direct path is reported to be of 1.21 eV. Hence, the energy barrier for H_2 splitting in the newly proposed mechanism is 0.13 eV lower [21]. Assuming that this mechanism can be applied to our system, we expect our value (1.00 eV) to be lowered by roughly the same order of magnitude (0.10 eV), which does not significantly affect the conclusions of our study. The activation of hydrogen leads to the final structures, which are exothermic by −2.31 eV (223 kJ mol^{-1}) over CeO_2 and −0.68 eV (66 kJ mol^{-1}) over Ga-containing CeO_2, in close agreement with Refs. [21,37]. As depicted in Fig. 4b, the final configurations are very different. Whereas pure ceria forms two equivalent OH groups, the gallium-containing surface generates stable OH and GaH species. The formation of GaH is in line with the IR results (*vide infra*) and indicates heterogeneous dissociation of H_2, forming H^+ and H^- ions. Thus, the incorporation of gallium appears to change the elementary steps of the reaction, by breaking hydrogen more efficiently than over pristine ceria.

However, this enhanced ability to activate hydrogen also influences the reducibility of the surfaces. The energy cost for the formation of an oxygen defect has been used as a reactivity index for assessing the reducibility of the ceria surface. In general, the lower the energy, the easier to form oxygen vacancies and the more reducible the catalyst is. The formation energy of O vacancies is 2.65 eV (254 kJ mol^{-1}) over CeO_2 and 1.45 eV (139 kJ mol^{-1}) over Ce-Ga oxide with a Ce:Ga = 97:3. This highlights that the promoted oxide is more prone to form defects, in line with the H_2-TPR and OSC data. It is thus expected that Ga-promoted ceria presents a higher number of oxygen vacancies than pure ceria in reaction conditions, as can be concluded from a thermodynamic DFT analysis shown in Fig. S2. The propensity to form oxygen vacancies is enhanced even more by the increased surface concentration of Ga. For example, it has been reported that the formation energy of defects is only 2.54 eV for a bulk supercell with composition $Ce_{24}Ga_8O_{60}$ (in the same conditions, bulk CeO_2 gives 3.23 eV and bulk Ga_2O_3 gives 4.00 eV) [25]. Whereas the improved activation of hydrogen is beneficial for applications of ceria in hydrogenation, the latter aspect is adverse, since all reaction intermediates are adsorbed on oxygen species [20]. Thus, these theoretical results already suggest that only by controlling the amount of promoter it is possible to achieve an optimal catalytic activity.

In order to validate these results, *in situ* infrared spectroscopy in DRIFT mode was conducted, monitoring the isothermal reduction of selected catalysts in H_2 flow. Prior to measurement, the pre-treatment at 623 K allowed us to remove most of the carbonates present on the samples. A (rather small) band assigned to carbonate species (1700–1200 cm^{-1}) still remains on the spectra after pre-treatment. Additionally, part of the surface hydroxyl groups (3000–3700 cm^{-1}) could not be removed. To properly clean the surface, a much higher pre-treatment temperature would be required, with the consequence of reducing the active surface area of the catalysts and dramatically affect the activity of the materials. Although such surface species might have an impact on the catalytic reactivity of ceria (as they reduce the total number of active sites), a slight discrepancy between the collected results and the performance of Ga-promoted ceria can be anticipated, as the influence of such surface groups is proportional to the exposed surface ceria. Fig. 5 shows the time evolution of the symmetry-forbidden $2f_{5/2} \rightarrow 2f_{7/2}$ electronic transition of Ce^{3+} (band at 2120 cm^{-1}) and the stretching mode of the GaH surface bond (band at 1960 cm^{-1}) [38,39]. Due to the low signal-to-noise ratio, only the results for $Ce_{90}Ga_{10}O_x$ and $Ce_{80}Ga_{20}O_x$ are shown. However, identical trends were obtained over catalysts with lower gallium content. In general, the concentration of GaH rapidly increases, reaching a maximal value, and then drops as the concentration of Ce^{3+} arises. This trend, confirmed also at higher temperature (Fig. S3), corroborates that gallium facilitates the dissociation of H_2 and the stabilization of atomic H species on the catalyst surface, as predicted by DFT. The GaH species are consumed, on the other hand, during the ceria reduction process, giving rise to Ce^{3+} species and, simultaneously, oxygen vacancies. Despite the very similar total surface area of $Ce_{80}Ga_{20}O_x$ and $Ce_{90}Ga_{10}O_x$ (100 and 108 $m^2\,g^{-1}$, respectively) which would point to an identical reducibility of the $Ce_{90}Ga_{10}O_x$ and $Ce_{80}Ga_{20}O_x$ samples in accordance with the literature [4], Fig. 5 shows that the IR band of Ce^{3+} in $Ce_{80}Ga_{20}O_x$ is approximately 1.5 times higher than that of $Ce_{90}Ga_{10}O_x$. Normalized to the surface amount of CeO_2 (Table 1), this factor is even higher (1.94). Therefore, the increased Ce^{3+} infrared signal over $Ce_{80}Ga_{20}O_x$ in comparison with that over $Ce_{90}Ga_{10}O_x$ is a clear indication of the increased amount of surface Ce^{3+}, which can be related to the higher (doubled) concentration of gallium. Notably, it would be helpful to be able to quantify the activation energy by infrared spectroscopy for the dissociation of H_2 on CeO_2. However, on cerium oxide, there are no elementary

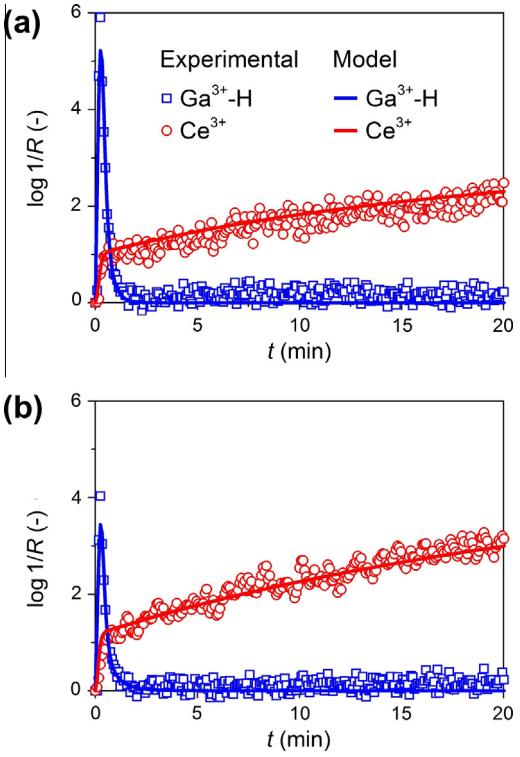

Fig. 5. Evolution of the concentration of the Ce^{3+} and Ga^3-H species over $Ce_{90}Ga_{10}O_x$ (a) and $Ce_{80}Ga_{20}O_x$ (b) monitored by diffuse reflectance infrared Fourier transform spectroscopy under flowing H_2 at 523 K.

steps that can be easily followed by IR as in the case of Ga-H formation.

The density functional theory simulations and the infrared spectroscopic results enable the postulation of a global H_2 activation mechanism, involving the key participation of Ga^{3+}-O surface groups in the hydrogenation [23–25]. This consists in the heterolytic splitting of H_2 to produce hydroxyl and GaH groups, which are responsible for the facile reduction of Ce^{4+} to Ce^{3+}:

$$Ga^{3+}{-}O + H_2 \rightarrow H{-}Ga^{3+}{-}OH \qquad \text{(step1)}$$

$$H{-}Ga^{3+}{-}OH + 2Ce^{4+} + OH^- \rightarrow Ga^{3+}{-}OH + 2Ce^{3+} + H_2O \qquad \text{(step2)}$$

The mechanism predicts that, as the reduction of Ce^{4+} progresses, the amount of Ga^{3+}–O sites able to chemisorb H_2 decreases. Thus, the generation of Ce^{3+}, with the concomitant formation of oxygen vacancies, leads to a decrease in the amount of available Ga^{3+}–O species. Using these steps as well as the direct reduction of Ce^{4+} by H_2 to Ce^{3+} and H_2O (step 3), a "lumped" microkinetic model describing the activation of H_2 on the promoted ceria was derived [23–25]. The solid lines in Fig. 5 represent the fitted evolution of the Ce^{3+} and GaH signals. Unfortunately, due to the low signal-to-noise ratio, the step 3 could not be determined independently at 523 K, as originally expected [25]. The stepwise model can be used to estimate the activation energy, the pseudo-first order kinetic constant, and initial reaction rate of the first step of the mechanism (Table 2). In particular, the energy required to split H_2 and form GaH (E_a (step 1) = 27 kJ mol^{-1}) is three times lower than that for the reduction of Ce^{4+} (E_a (step 2) = 87 kJ mol^{-1} or E_a (step 3) = 92 kJ mol^{-1}).

Table 2
Parameters obtained from the microkinetic analysis of the H_2 activation mechanism on the gallium-promoted ceria catalysts.

Sample	E_a (step 1) (kJ mol^{-1})	E_a (step 2) (kJ mol^{-1})	k_1 (423 K) (mmol h^{-1} g_{sites}^{-1} nm^2)	r_1^0 (423 K)[a] (mmol h^{-1} g^{-1})
$Ce_{90}Ga_{10}O_x$	26.8	87.9	68.0	8.0
$Ce_{80}Ga_{20}O_x$	27.6	87.1	83.7	11.5

[a] Initial reaction rate for H_2 dissociation on the Ga-O sites.

4.3. Hydrogenation of alkynes

The catalysts were tested in the gas-phase hydrogenation of acetylene and methylacetylene. The top part of Fig. 6 depicts the influence of temperature on the activity and olefin selectivity of CeO_2 and $CeGaO_x$. The turnover frequency over pure CeO_2 shows the previously reported volcano behavior [13], increasing when the temperature increases from 323 to 473 K, reaching its maximum, and abruptly decreasing at higher temperatures. This drop is due to the extensive reduction of the ceria surface [13]. The trend over $Ce_{95}Ga_5O_x$ is similar; however, the maximal activity in both reactions occurs at a lower temperature (423 K). This correlates well with the H_2-TPR characterization, displaying a 50 K decrease in the temperature at which the Ga-containing material begins to be reduced (Fig. 1b). Therefore, the easier reducibility of $CeGaO_x$ leads to a drop in activity at lower temperature. This shift is accompanied by an increase in reactivity. In fact, fixing the TOF at 60×10^{-3} h^{-1}, the Ga-containing catalyst attains the same acetylene and methylacetylene hydrogenation activity of CeO_2 at a 100 K lower temperature, which points to the occurrence of less surface reduction over the Ce-Ga solid solution at low temperature. Since pure Ga_2O_3 was catalytically inactive at all conditions, this result confirms that the presence of gallium into the ceria lattice is responsible for the improved activity of CeO_2. From the data in Fig. 6a, in the temperature range of 323–423 K (where no surface reduction is observed), it is possible to estimate the apparent activation energy of the catalysts in acetylene hydrogenation, leading to values of 33 kJ mol^{-1} for CeO_2 and 18 kJ mol^{-1} for $Ce_{95}Ga_5O_x$ (Fig. S4). The discrepancy between the experiment and the DFT-calculated values is not fully clear at this point but can be related to the temperature and pressure gaps of the calculations and to the choice of a model surface, without considering the presence of more reactive ((1 1 0) and (1 0 0)) or stepped (2 1 1) facets responsible for an easier H_2 dissociation [22]. Nevertheless, the reduced activation energy of $CeGaO_x$ with respect to CeO_2 verifies that Ga partakes in the activation mechanism of hydrogen.

The bottom part of Fig. 6 shows the influence of the feed hydrogen-to-alkyne ratio on the activity and olefin selectivity of CeO_2 and $CeGaO_x$ in acetylene and methylacetylene hydrogenation. The turnover frequency in both reactions increases linearly with the inlet partial pressure of hydrogen. The selectivity to ethylene in acetylene hydrogenation increases from 78% (at H_2:C_2H_2 = 10) to 80% (at H_2:C_2H_2 = 30) over CeO_2 and from 83% (at H_2:C_2H_2 = 10) to 95% (at H_2:C_2H_2 = 30) over $Ce_{95}Ga_5O_x$, indicating that the promotion with Ga suppresses undesired pathways in acetylene hydrogenation. The selectivity to propene in methylacetylene hydrogenation remains mostly unchanged at 95–97% over pure and promoted ceria.

Fig. 7 highlights the product distribution at selected reaction conditions over CeO_2 and $Ce_{95}Ga_5O_x$. Oligomers comprise the main secondary product in acetylene and methylacetylene hydrogenation and are favored at high temperature and low hydrogen coverage (H_2:C_2H_2 = 10). The selectivity to the over-hydrogenated hydrocarbon over CeO_2 does not exceed 8% in acetylene hydrogenation and 4% in methylacetylene hydrogenation, despite the high H_2 content in the feed. Over $CeGaO_x$, the alkane selectivity is constantly less than 2%. Upon co-feeding of the olefin in acetylene hydrogenation (Fig. 8), the $Ce_{95}Ga_5O_x$ catalyst retains the remarkably high ethylene selectivity (86%), and the remaining products were oligomers (13%) and ethane (<1%). The evident drop in

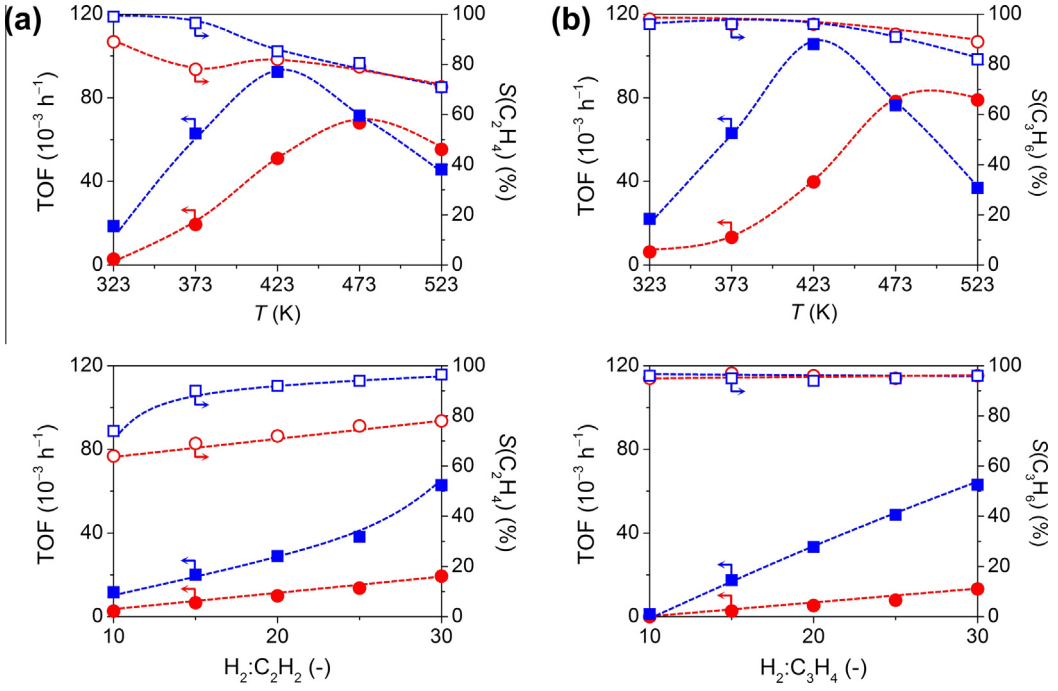

Fig. 6. Turnover frequency and ethylene selectivity as a function of temperature (top) and H_2:alkyne ratio (bottom) in acetylene (a) and methylacetylene (b) hydrogenation over CeO_2 (red circles) and $Ce_{95}Ga_5O_x$ (blue squares). The influence of temperature on the activity and product selectivity was studied at H_2:alkyne = 30, while the influence of H_2:alkyne ratio was assessed at T = 373 K. Other conditions: τ = 0.3 s and P = 1 bar. (For the interpretation of the references to color in this figure legend, the reader is referred to the Web version of this article.)

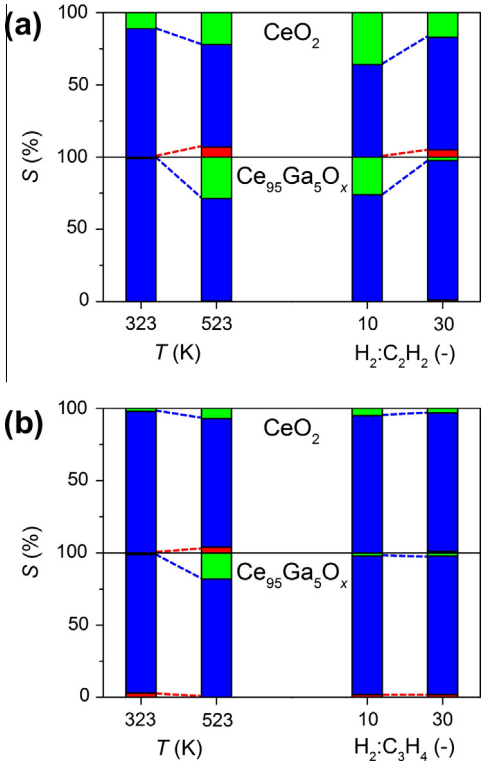

Fig. 7. Selectivity to alkene (blue), alkane (red), and oligomers (green) in acetylene (a) and methylacetylene (b) hydrogenation. The turnover frequency at each condition can be deduced from Fig. 6 and the experimental conditions are detailed in the caption of the same figure. (For the interpretation of the references to color in this figure legend, the reader is referred to the Web version of this article.)

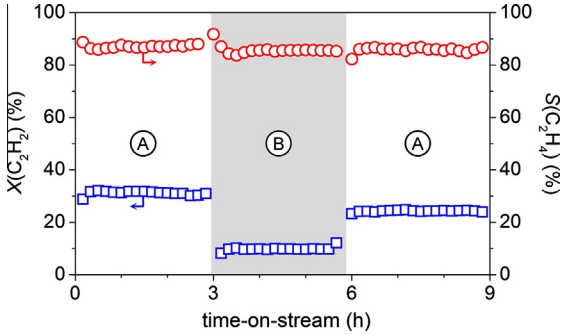

Fig. 8. Acetylene conversion (squares) and ethylene selectivity (circles) over $Ce_{95}Ga_5O_x$ versus time-on-stream. The reaction was performed at $T = 423$ K, $\tau = 0.3$ s, and $P = 1$ bar in different feed mixtures: (A) 2.5 vol.% C_2H_2, 75 vol.% H_2 and (B) 2.5 vol.% C_2H_2, 10 vol.% C_2H_4, and 75 vol.% H_2. He was the balance gas.

activity during C_2H_2 hydrogenation in excess ethylene is due to the competitive adsorption of ethylene and acetylene on the catalyst, as demonstrated in earlier reports [20]. Additional tests over CeO_2 and $Ce_{95}Ga_5O_x$ in mixtures of ethylene and hydrogen or propylene and hydrogen have further confirmed the inactivity of the sample in alkene hydrogenation in the range of conditions investigated. This has been ascribed to the large energy barriers for the over-hydrogenation steps over ceria-based catalysts [20,40].

Figs. 9 and S5 depict the performance of the CeO_2-based catalysts with variable Ga content. The figure indicates that there is an optimum in the concentration of gallium in the sample. In fact, materials with a low Ga content (Ga:(Ce + Ga) < 0.02) hardly excel the performance of non-promoted ceria because of the insufficient influence of Ga on lowering the H-H bond cleavage; at high content of Ga (Ga:(Ce + Ga) > 0.10), the extensive surface reduction leading

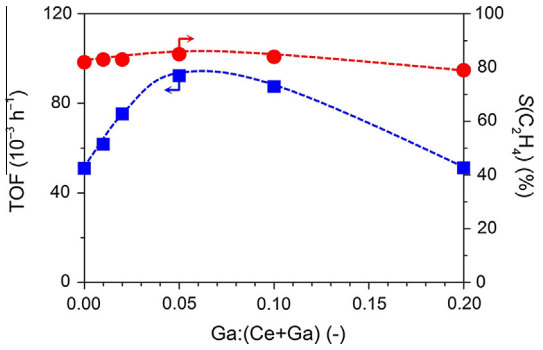

Fig. 9. Turnover frequency (solid symbols) and ethylene selectivity (open symbols) in acetylene hydrogenation as a function of Ga content in the ceria catalysts. Conditions: $T = 423$ K, $H_2:C_2H_2 = 30$, $\tau = 0.3$ s, and $P = 1$ bar.

to oxygen removal has an adverse effect on the performance. The activity enhancement of the Ga-containing sample is not caused by the preparation method. In fact, as depicted in Fig. S6, by preparing the $Ce_{95}Ga_5O_x$ catalyst via solid-state synthesis followed by calcination at high temperature, we were able to obtain a solid solution, as confirmed by the shift in the XRD reflections. Applied in acetylene hydrogenation, the material was still more active and selective than CeO_2.

4.4. Role of Ga in CeO_2 catalyzed hydrogenation

Experimental and theoretical results evidence that gallium enhances the hydrogenation performance by providing an alternative mechanism of hydrogen splitting to the reaction pathway on pure ceria [20,21]. This mechanism involves the formation of surface hydride species on the Ga-containing sample. The selection of a trivalent cation as promoter, such as Ga, appears to be crucial for enhancing the ceria activity, since these metals create a lattice strain, increasing the distance between O-O and enlarging the diffusion path of mobile ions [41]. In order to assess the importance of the H_2 dissociation step to rationalize the catalytic results, we have calculated the energy profile by DFT for the partial hydrogenation of acetylene to ethylene (Fig. S7), considering only the thermodynamic stability of the intermediates reported in the literature [20] and assuming that the transition structures over pure and promoted ceria are similar, both in geometry and in energy. The obtained profile is very similar on pure and Ga-promoted ceria in the steps involving organic moieties. The splitting of the H-H bond seems to be the only step in the mechanism being affected by the presence of gallium. Besides, the degree of reduction of the ceria slabs was found to be irrelevant for the H_2 dissociation step and for the acetylene hydrogenation pathway, since this only influences the total number of active sites. In fact, the energy barrier for H_2 dissociation is *ca.* 1 eV on both stoichiometric and reduced CeO_2 [20] (Table S2 and Fig. S7).

Because of their efficiency in activating hydrogen, the Ga-promoted samples are also more prone to surface reduction and, as confirmed by H_2-TPR, more easily form oxygen vacancies. The latter are known to be detrimental for the hydrogenation activity [13]. Therefore, an optimal catalytic process over promoted cerias can be engineered by tuning the surface gallium concentration in the mixed oxide and the operating conditions. High Ga contents and temperatures are adverse due to the excessive formation of oxygen vacancies. We found an optimal catalyst composition at a molar Ce:Ga ratio of 95:5, in which the benefit of the improved H_2 activation by gallium surpasses the concomitant increase of oxygen vacancies, leading to a net catalytic benefit. Therefore, we believe that it is not wise to derive structure–performance relationships of ceria catalysts by simply comparing the reducibility

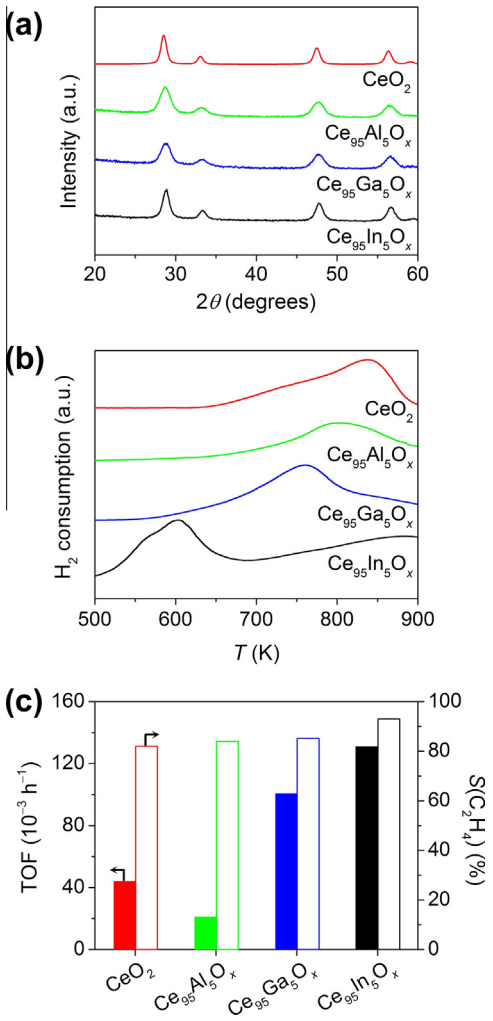

Fig. 10. X-ray diffraction patterns of different promoted ceria catalysts (a), temperature-programmed reduction in H_2 (b), and turnover frequency and ethylene selectivity of different promoted ceria catalysts in acetylene hydrogenation (c). Conditions: T = 423 K, H_2:C_2H_2 = 30, τ = 0.3 s, and P = 1 bar.

and oxygen storage properties of various samples at a defined temperature. Because of the dynamic redox properties of CeO_2, at high temperature, the Ga-promoted oxides show higher OSC than pure ceria. As the OSC is linked to the amount of surface vacancies, it might appear that the Ga-containing samples are not appropriate for applications in hydrogenation catalysis. However, it is only by comparing the OSC of the various samples at the temperature where each catalyst attains the optimal activity that it is possible to acquire a flavor of the hydrogenation behavior.

4.5. Extrapolation to other metals

Since the promotion effect observed over the $CeGaO_x$ oxides appears to be directly linked to the enhanced reducibility of ceria, based on this descriptor, we have assessed the role of other metals in promoting the catalytic behavior of ceria in hydrogenation. Particularly, we have prepared ceria-based samples containing aluminum ($CeAlO_x$) and indium ($CeInO_x$), using a Ce:promoter ratio of 95:5. Characterization of the samples by XRD (Fig. 10a) reveals characteristic reflections which are indexed to the fluorite structure of ceria. The average crystallite size is *ca.* 7 nm for $Ce_{95}Al_5O_x$ and 12 nm for $Ce_{95}In_5O_x$, in line with the low total surface area of the latter sample (Table 1). From the XRD patterns, it is possible to estimate the lattice parameters of $Ce_{95}In_5O_x$ (a_{cell} = 0.5385 nm) and $Ce_{95}Al_5O_x$ (a_{cell} = 0.5407 nm), in comparison with that of CeO_2 (a_{cell} = 0.5463 nm); the shrinkage of the lattice for the In-promoted sample confirms the penetration of the In^{3+} cations into fluorite lattice of CeO_2. On the other hand, the similarity between the lattice parameters of $Ce_{95}Al_5O_x$ and CeO_2 points to the formation of separated Al_2O_3 particles. The surface Ce:(Ce + Al) ratio determined by XPS (Table 1) differs from the corresponding bulk value, supporting a non-homogeneous distribution of aluminum. This might be related to the size of the cations ($r(Al^{3+})$ = 67 pm and $r(In^{3+})$ = 94 pm in octahedral 6-coordinate configuration) and suggests that cations that are remarkably different in size compared to Ce^{4+} ($r(Ce^{4+})$ = 101 pm) cannot easily penetrate into the fluorite lattice. H_2-TPR (Fig. 10b) confirms these results, showing the shift to lower temperature over $Ce_{95}In_5O_x$, which could not be observed over the Al-containing samples. The catalytic data in Fig. 10c nicely correlate with the H_2-TPR shift, indicating that the In-containing sample is even more active and selective than the gallium-promoted catalyst.

5. Conclusions

We have demonstrated that gallium enhances the activity of ceria in the semi-hydrogenation of acetylene and methylacetylene. The characterization of mixed Ce-Ga oxides prepared by co-precipitation or solid-state synthesis reveals that the progressive incorporation of gallium into the ceria structure, forming a solid solution, boosts the oxygen storage capacity and the reducibility of the material. This is ascribed to the facilitated H_2 activation on the Ga-containing samples, which leads to an enhanced catalytic activity. The presence of gallium does not appear to modify any other elementary step of the reaction. The interplay between the advantage brought by the decreased barrier for H_2 cleavage and the disadvantage arising from the increased number of oxygen vacancies governs the reactivity of the $CeGaO_x$ catalysts in alkyne hydrogenation, finding an optimum at a molar Ce:Ga ratio of 95:5. The remarkable selectivity of the mixed oxide to ethylene or propylene (80–97%) was preserved when excess alkene was added to the feed. Indium was also identified as an effective promoter, following the same mechanistic principle as gallium. This work comprises the first application of promoted cerias in hydrogenation catalysis, leading to a temperature reduction for the gas-phase alkyne semi-hydrogenation from 473 K (CeO_2) to 373 K ($Ce_{95}Ga_5O_x$ and $Ce_{95}In_5O_x$).

Acknowledgments

Dr. Frank Krumeich and the Scientific Center for Optical and Electron Microscopy (ScopeM) of ETH Zurich are thanked for the microscopy studies. The DFT calculations were performed using HPC resources from GENCI-CINES/IDRIS (Grants 2014-x2014082131) and from CCRE-DSI of the University P.M. Curie, Paris. J.V., M.B., S.C., and A.B. thank CONICET, UNL (PI 501 201101 00311), MINCYT (Eulanest 042), and ANPCyT (PICT 2012-1280, PME 2003-8, and PME 2006-311) for financial support. The COST Action CM 1104 is also acknowledged.

Appendix A. Supplementary material

Supplementary data associated with this article can be found, in the online version, at http://dx.doi.org/10.1016/j.jcat.2015.01.020.

References

[1] F. Yang, J. Graciani, J. Evans, P. Liu, J. Hrbek, J.F. Sanz, J.A. Rodriguez, J. Am. Chem. Soc. 133 (2011) 3444.

[2] D.Y. Wang, Y.J. Kang, V. Doan-Nguyen, J. Chen, R. Kungas, N.L. Wieder, K. Bakhmutsky, R.J. Gorte, C.B. Murray, Angew. Chem., Int. Ed. 50 (2011) 4378.
[3] A.P. Amrute, C. Mondelli, M. Moser, G. Novell-Leruth, N. López, D. Rosenthal, R. Farra, M.E. Schuster, D. Teschner, T. Schmidt, J. Pérez-Ramírez, J. Catal. 286 (2012) 287.
[4] E. Aneggi, D. Wiater, C. de Leitenburg, J. Llorca, A. Trovarelli, ACS Catal. 4 (2014) 172.
[5] J.A. Rodriguez, S. Ma, P. Liu, J. Hrbek, J. Evans, M. Pérez, Science 318 (2007) 1757.
[6] J. Graciani, K. Mudiyanselage, F. Xu, A.E. Baber, J. Evans, S.D. Senanayake, D.J. Stacchiola, P. Liu, J. Hrbek, J. Fernández Sanz, J.A. Rodriguez, Science 345 (2014) 546.
[7] M.V. Ganduglia-Pirovano, J.L.F. Da Silva, J. Sauer, Phys. Rev. Lett. 102 (2009) 026101.
[8] H.L. Tuller, A.S.J. Nowick, Electrochem. Soc. 122 (1975) 255.
[9] J. Paier, C. Penschke, J. Sauer, Chem. Rev. 113 (2013) 3949.
[10] E.W. McFarland, H. Metiu, Chem. Rev. 113 (2013) 4391.
[11] B.M. Reddy, P. Bharali, P. Saikia, A. Khan, S. Loridant, M. Muhler, W. Grünert, J. Phys. Chem. C 111 (2007) 1878.
[12] R. Farra, M. García-Melchor, M. Eichelbaum, M. Hashagen, W. Frandsen, J. Allan, F. Girgsdies, L. Szentmiklósi, N. López, D. Teschner, ACS Catal. 3 (2013) 2256.
[13] G. Vilé, B. Bridier, J. Wichert, J. Pérez-Ramírez, Angew. Chem., Int. Ed. 51 (2012) 8620.
[14] G. Vilé, S. Wrabetz, L. Floryan, M.E. Schuster, F. Girgsdies, D. Teschner, J. Pérez-Ramírez, ChemCatChem 6 (2014) 1928.
[15] D. Teschner, J. Borsodi, A. Wootsch, Z. Révay, M. Hävecker, A. Knop-Gericke, S.D. Jackson, R. Schlögl, Science 320 (2008) 86.
[16] J.A. Anderson, J. Mellor, R.P.K. Wells, J. Catal. 261 (2009) 208.
[17] F. Studt, F. Abild-Pedersen, T. Bligaard, R.Z. Sørensen, C.H. Christensen, J.K. Nørskov, Science 320 (2008) 1320.
[18] M. Armbrüster, K. Kovnir, M. Behrens, D. Teschner, Y. Grin, R. Schlögl, J. Am. Chem. Soc. 132 (2010) 14745.
[19] Y. Segura, N. López, J. Pérez-Ramírez, J. Catal. 247 (2007) 383.
[20] J. Carrasco, G. Vilé, D. Fernández-Torre, R. Pérez, J. Pérez-Ramírez, M.V. Ganduglia-Pirovano, J. Phys. Chem. C 118 (2014) 5352.
[21] M. García-Melchor, N. López, J. Phys. Chem. C 118 (2014) 10921.
[22] G. Vilé, S. Colussi, F. Krumeich, A. Trovarelli, J. Pérez-Ramírez, Angew. Chem., Int. Ed. 53 (2014) 12069.
[23] S. Collins, G. Finos, R. Alcántara, E. del Rio, S. Bernal, A. Bonivardi, Appl. Catal., A 388 (2010) 202.
[24] P. Quaino, L. Siffert, O. Syzgantseva, F. Tielens, C. Minot, M. Calatayud, Chem. Phys. Lett. 519–520 (2012) 69.
[25] J. Vecchietti, S. Collins, W. Xu, L. Barrio, D. Stacchiola, M. Calatayud, F. Tielens, J.J. Delgado, A. Bonivardi, J. Phys. Chem. C 117 (2013) 8822.
[26] G. Kresse, J. Hafner, Phys. Rev. B 47 (1993) 558.
[27] G. Kresse, J. Hafner, Phys. Rev. B 49 (1994) 14251.
[28] G. Kresse, J. Furthmüller, Phys. Rev. B 54 (1996) 11169.
[29] J.P. Perdew, K. Burke, M. Ernzerhof, Phys. Rev. Lett. 77 (1996) 3865.
[30] P.E. Blochl, Phys. Rev. B 50 (1994) 17953.
[31] G. Kresse, D. Joubert, Phys. Rev. B 59 (1999) 1758.
[32] S.L. Dudarev, G.A. Botton, S.Y. Savrasov, C.J. Humphreys, A.P. Sutton, Phys. Rev. B 57 (1998) 1505.
[33] G. Henkelman, B.P. Uberuaga, H. Jónsson, J. Chem. Phys. 113 (2000) 9901.
[34] B.M. Weckhuysen, D.E. Keller, Catal. Today 78 (2003) 25.
[35] Y. Zhang, S. Andersson, M. Muhammed, Appl. Catal., B 6 (1995) 325.
[36] S. Zhao, R.J. Gorte, Appl. Catal., A 248 (2003) 9.
[37] D. Fernández-Torre, J. Carrasco, M.V. Ganduglia-Pirovano, R. Pérez, J. Chem. Phys. 141 (2014) 014703.
[38] C. Binet, A. Badri, L.-C. Lavalley, J. Phys. Chem. 98 (1994) 6392.
[39] S.E. Collins, M.A. Baltanás, A.L. Bonivardi, Langmuir 21 (2005) 962.
[40] M. García-Melchor, L. Bellarosa, N. López, ACS Catal. 4 (2014) 4015.
[41] M. Calatayud, A. Markovits, M. Menetrey, B. Mguig, C. Minot, Catal. Today 85 (2003) 12.